

## Numerical Simulations of Flow in a 3-D Supersonic Intake at High Mach Numbers

R. Sivakumar and V. Babu

*Indian Institute of Technology Madras, Chennai-600 036*

### ABSTRACT

Numerical simulations of the compressible, 3-D non reacting flow in the engine inlet section of a concept hypersonic air-breathing vehicle are presented. These simulations have been carried out using FLUENT. For all the results reported, the mesh has been refined to achieve area-averaged wall  $y+$  about 105. Mass flow rate through the intake and stagnation pressure recovery are used to compare the performance at various angles of attack. The calculations are able to predict the mode of air-intake operation (critical and subcritical) for different angles of attack. Flow distortion at the intake for various angles of attack is also calculated and discussed. The numerical results are validated by simulating the flow through a 2-D mixed compression hypersonic intake model and comparing with the experimental data.

**Keywords:** Numerical simulations, mass flow rate, flow distortion, bowshock, cowl shock, cowl lip

### 1. INTRODUCTION

The design of the inlet is of great importance for the performance of future hypersonic space transportation planes powered by air-breathing engines. Since these engines do not have any moving parts, the air that enters the engine has to be compressed completely in the inlet. Thus, it is imperative that this compression process be as efficient as possible. The key performance parameters of the inlet are total pressure recovery and mass flow rate.

Optimisation of the inlet performance can lead to a remarkable gain in the maximum payload of the vehicle. The distinguishing feature of a hypersonic air-breathing engine is that the flow is still supersonic at the end of the inlet section and before the entry into the combustor. The dominating phenomenon in hypersonic inlet flow is the interaction of oblique

shocks induced by the inlet ramps with the boundary layer developing on the inlet walls. An impinging shock may force the boundary layer to separate from the wall, resulting in total pressure recovery losses and a reduction of the inlet efficiency. Fixed-geometry inlets can be used only over a relatively narrow range of Mach numbers while variable-geometry inlets can be used over a wide range of Mach numbers with reasonably good pressure recovery. The use of a sophisticated variable geometry simplifies the aerodynamic design of the inlet.

Gaitonde and Shang<sup>1</sup> noted that forebodies of the proposed hypersonic aircraft had ramp-like structures designed to compress the incoming air with oblique shock waves. The forebodies, therefore, act as the compressor system for the inlet. Compression shocks may form a relatively strong oblique shock in conjunction with the vehicle bowshock. For optimum

mass flow through the inlet, it is desirable that these shocks be positioned so as to converge on the inlet cowl-leading edge where these interact with the bowshock produced by the cowl lip. Viscous hypersonic shock-on-shock interactions can significantly affect the performance of the inlet through the creation of anomalous pressure and heat-transfer peaks on the cowl-leading edge. The schematic hypersonic intake flow field shown in their paper depicts three shock waves that interact on the cowl lip<sup>1</sup>: (i) the bowshock wave produced by the cowl lip, (ii) the bowshock wave originating at the vehicle leading edge, and (iii) an oblique shock wave produced by the compressive turning of the flow by the inlet ramp<sup>1</sup>.

Schulte<sup>2</sup>, *et al.* demonstrated the possibilities of manipulating shock/boundary layer interactions with possible utilisation in hypersonic inlets. The shock from the cowl tip induces separation of the boundary layer on the ramp wall, leading to a separation bubble. At the beginning of the separation region, the flow is redirected due to the shape of the bubble, and similar to the flow over a ramp, a shock (designated as separation shock) is induced. The separation bubble is thickest at the point of impingement of the cowl shock. Further downstream at the reattachment point, flow redirection induces a so-called reattachment shock. Experimental as well as numerical investigations of a model hypersonic inlet were undertaken by Schneider and Koschel<sup>3</sup> to evaluate the possibilities to influence the shock/shock and shock/boundary layer interaction by the design of suitable inlet geometry, and thus avoiding bleed systems.

Falempin and Montazel<sup>4</sup> conducted both theoretical and experimental studies to determine the characteristics of a 2-D inlet with external/internal compression for free stream Mach numbers ranging from 2 to 8. Goldfeld<sup>5</sup>, *et al.* presented an experimental study of a scramjet module consisting of a 3-D inlet followed by a combustion chamber. The module was designed to study the flow structure, to obtain the inlet characteristics, and to study the mutual effects of the combustion of the inlet. Reddy and Weir<sup>6</sup> carried out numerical calculations of the flow field in the Mach No. 5 inlet using the PARC3D code and compared the results with the experimental

data. The PARC3D code is a full Navier-Stokes time-marching code, and was earlier used for simulating the flow in 3-D supersonic and 2-D hypersonic flow configurations. PARC3D solves the full 3-D Reynolds-averaged Navier-Stokes equations. Effects such as bleeding on the inlet walls were also included. Static pressure on the ramp surface along the centreline and 7.5 inch from the centreline were compared with the experimental data and found a good agreement between the two.

Bezgin, *et al.* investigated the CFD support in the development of Hypersonic Flight Laboratory (HFL) and the modeling of a scramjet engine. They used the SUPNEF code for optimising the scramjet duct. It was a fast code based on parabolised Navier-Stokes equations without wall boundary layer effects, and quite useful for the initial estimations. The influence of viscosity effects on the flow parameters in 3-D inlet of model scramjet integrated with HFL forebody was evaluated. The numerically obtained data at the exit of the inlet section was used for the predictions of the combustor operation in flight conditions.

Emami<sup>8</sup>, *et al.* presented inlet-isolator test data result with variations in both geometry (isolator length and rearward-facing step height) and flow field properties (boundary layer thickness and oblique glancing sidewall shock interaction). The test was conducted for a total of 250 geometric configurations. The Mach number for their investigation was 4.03. The measured streamwise centreline Mach number distributions, and consequently the centreline static pressure distribution, showed temporally steady, spatially oscillatory behaviour with gradual dampening from supersonic to subsonic flow through the shock trains. The results show that the combined inlet-isolator maximum back pressure capability increased with increasing both the isolator length and inlet contraction ratio, while it was decreased by inlet distortion and an increase in the area of the rearward-facing step isolator.

The objective of the present study is to carry out well resolved, 3-D compressible flow calculations in a realistic inlet geometry and establish the viability of numerical simulations as a design tool. Performance metrics such as mass flow rate, total pressure

recovery, and flow distortion have been evaluated and different modes of operation of the intake have also been simulated.

## 2. COMPUTATIONAL METHODOLOGY

The cross-sectional view of the intake along with the complete engine is shown in Fig. 1. All the dimensions have been nondimensionalised using the height  $H$  of the intake entry section. The engine was a scramjet engine being considered for a concept hypersonic vehicle. The operating conditions for the vehicle were as follows:

There are four ramps (indicated with crosses in Fig. 1) on the body side for external/internal compression of the flow by means of oblique shocks. The inlet section of the engine is a converging passage to achieve internal compression of the supersonic flow. The constant area passage following this is the combustor isolator.

The variable-area combustor is located beyond the isolator section. The Mach number at the inlet to the combustor is desired to be in between 2.0 and 2.5. In the present study, the geometry was truncated at the combustor inlet and non reacting flow calculations were carried out. Further, computations were performed in one-half of the cross-section as the engine was symmetric about the vertical ( $y = \text{constant}$ ) midplane. The flow through the engine was compressible and three-dimensional. Although the free-stream Mach number was in the hypersonic range, real-gas effects were negligible since the Knudsen numbers were quite low at the operational altitude\*. Air is the working fluid and it was taken to be a mixture of  $O_2$  and  $N_2$  with mass fractions 0.23 and 0.77, respectively. Viscosity and constant

value ( $C_p$ ) of the mixture were evaluated using mass weighted averaging. For the individual species, these properties were calculated using Sutherland's law and fifth-order polynomials in temperature, respectively.

The one-equation Spalart-Allmaras model that solves a modelled transport equation for the kinematic eddy (turbulent) viscosity was used in the present calculations. This model embodies a relatively new class of one-equation models in which it is not necessary to calculate a length scale related to the local shear layer thickness. It is designed specifically for aerospace applications involving wall-bounded flows and has been shown to give good results for boundary layers subjected to adverse pressure gradients. For 3-D flows, the use of a one-equation model over two-equation models can result in considerable savings in computational efforts.

With this in mind, in the present work, the Spalart-Allmaras model has been used for the 3-D calculations and the  $k-\epsilon$  model for the 2-D calculations.

## 3. BOUNDARY CONDITIONS

The boundaries in the computational domain fall into one of the two categories, namely solid or fluid. Accordingly, additional conditions need to be specified on these boundaries. In the present study, standard wall functions and adiabatic conditions have been used on all-solid surfaces. The latter tends to over-predict the temperature, but is used here, owing to the absence of any data on the heat-transfer coefficient. Turning to the fluid boundaries, there are six of these, namely inlet and outlet ( $x = \text{constant}$  planes), top and bottom ( $z = \text{constant}$

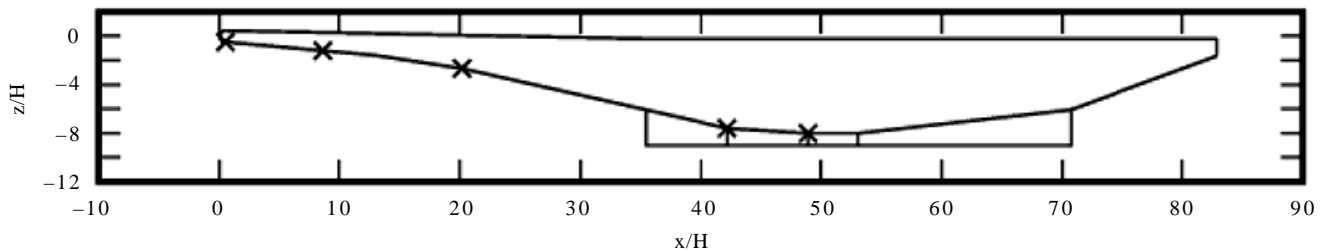


Figure 1. Cross-sectional view of the 3-D intake on the symmetry plane.

\* From the equation of state  $p = nkT$ , the number density at the operating altitude can be calculated as  $2.61 \times 10^{23}$  particles/m<sup>3</sup>. Assuming that the mean free path  $\lambda \sim 1/n^{1/3}$ , it can be seen that  $\approx 1.57 \times 10^{-8}$  m/s. With the characteristic dimension being of the order of a meter, the Kundsen number thus works out to be  $O(10^{-8})$

planes) and front and back ( $y = \text{constant}$  planes). Each of these boundaries is now considered in turn.

As the flow is supersonic at the inlet, all the flow variables were specified. Accordingly, free-stream stagnation and static pressure, stagnation temperature and  $X$  and  $Z$  components of flow direction were specified. The values  $X$  and  $Z$  components of flow direction vary depending upon the angle of attack. In the present study, the angle of attack was varied from  $4^\circ$ – $12^\circ$ . All the flow variables at the outlet boundary, including pressure, were determined from the interior of the domain by extrapolation, since the flow is supersonic here.

Far-field boundary conditions, namely free-stream static pressure, static temperature, Mach number, and  $X$  and  $Z$  components of flow direction were imposed on the top and bottom boundaries. To effectively approximate true infinite-extent conditions, the far-field boundary should be sufficiently far away from the engine.

After a few trials, it was decided to place these boundaries at a distance equal to 2.5-time the height of the engine from the nearest engine surface. This is justified *a posteriori* by examining the contours of Mach numbers and other variables to ensure that the free-stream conditions were satisfied on these boundaries.

The front boundary is a symmetry boundary and hence normal velocity and normal gradients of all the variables were set to zero. At the back boundary, far-field boundary conditions were specified in a manner similar to the top and bottom boundaries. This boundary was placed at a distance equal to 5-time the height of the engine, from the nearest engine surface. The 3-D numerical simulations were carried out using the commercial software FLUENT. The coupled solver available in FLUENT was used for all the calculations with explicit time stepping.

#### 4. VALIDATION STUDY

As reliable data, either experimental or numerical, for 3-D supersonic intakes was not available in the open literature, validation studies were carried out for a 2-D geometry for which experimental data was available.

The mixed-compression hypersonic intake model shown in Fig. 2, investigated experimentally by Schneider and Koschel<sup>3</sup> has been considered here. The  $k$ - $\varepsilon$  model with standard wall functions was used for these 2-D calculations. The computational domain along with the boundary conditions employed is shown in Fig. 2.

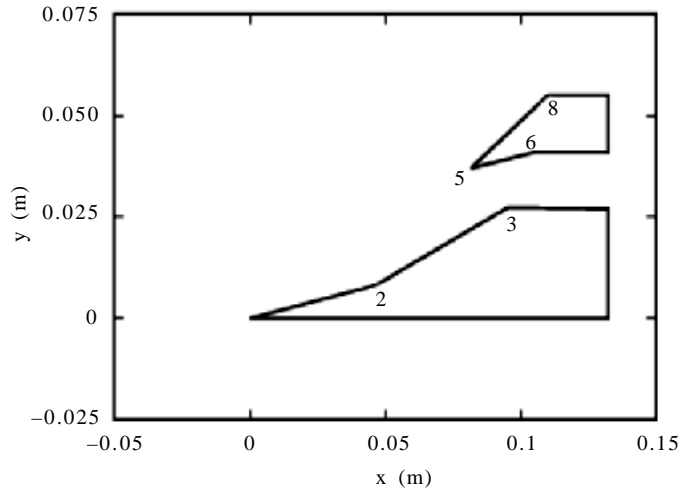


Figure 2. Geometry of the 2-D intake<sup>3</sup>.

An unstructured grid with quadrilateral/triangular cells was used for these calculations. The top and bottom boundaries were at a distance equal to 13 and 0.5 times the height of the engine, respectively from the nearest solid surface. The top boundary was so placed as to avoid intersecting the leading edge shock. The operating conditions used in the experiments were as follows:

Calculations initially were carried out on a mesh with 79729 cells. This grid was then refined successively. Firstly, adaption based on the gradient of the static pressure was done, so that the shocks could be captured accurately. Secondly, refinement near all the no-slip surfaces so as to achieve wall  $y+$  values  $< 30$  was done to resolve the boundary layers. This resulted in grids with 99979 and 119098 cells. The maximum value for the wall  $y+$  values for the three grids are approximately 60, 40, and 30, respectively. So it can be concluded that the grid with 119098 is adequately able to resolve the flow field. All the solutions discussed here have been obtained on the grid.

The calculations were carried out till the residuals for all the equations, viz., continuity, two components

of momentum, energy,  $k$  and  $\varepsilon$  were  $< 10^{-3}$ . Even with gradient-based adaption, it proved to be impossible to get the residuals in the vicinity of certain points on the shock fronts below  $10^{-3}$ . The area-averaged residuals, however, were of the order of  $10^{-5}$  or less. The difference between the mass flow rates at the inlet and exit was about 0.0052 kg/s (less than 0.1% of the mass flow rate through the inlet).

Contours of Mach number for this intake geometry are shown in Fig. 3. Oblique shocks originating at compression corners 1 and 2 and the expansion fan at corner 3 can be clearly seen in this figure. Furthermore, these oblique shocks coalesce with the oblique shock generated at corner 5 and form a strong oblique shock ahead of the leading face of the lip. Expansion fan around corner 6 on the upper side as well as high and low pressure cells in the interior from multiple reflected shocks and expansion waves are visible in this figure.

As the oblique shock from corner 2 does not terminate at the lip corner (number 5), there is spillage over and around the lip and so the intake is operating in a subcritical mode for this value of free-stream Mach number. The ratio of the stagnation pressure at the exit to the free-stream stagnation

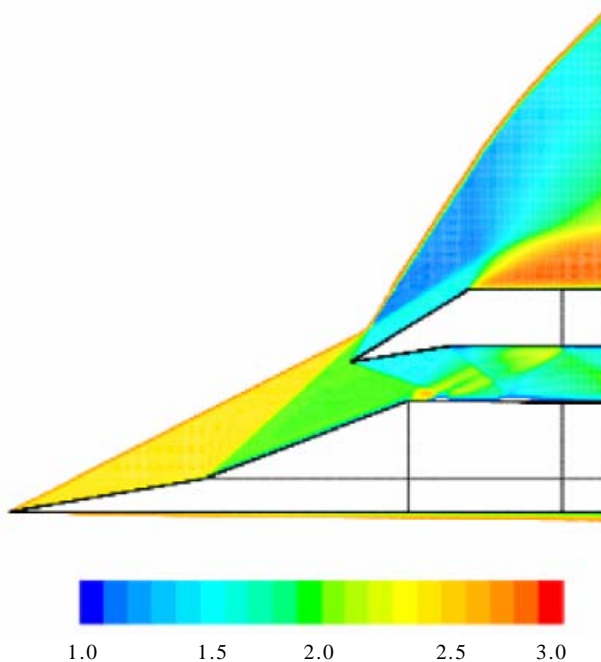


**Figure 3. Contours of Mach number.**

pressure is 0.727, which is lower than the value of 0.89 predicted by inviscid analysis for this intake. This is to be expected, as the present calculations are fully viscous.

Pathlines of particles released from the left computational boundary and coloured by the static pressure (made dimensionless with free-stream stagnation pressure) are shown in Fig. 4. This figure vividly shows the oblique shock fronts and the expansion fans as well as the flow turning and the corresponding pressure rise/fall. The pathlines inside the intake show the oblique shock wave from the cowl lip (corner 5) and the expansion fan around corner 8 on the outside surface. The undulations in the pathlines inside the intake are the result of reflected shock/expansion waves. For critical operation of the intake, the height of the capture area would simply be the height of corner 5, and the corresponding mass flow rate is 9.979 kg/s. The actual mass flow rate through the engine for the specified operating condition comes out to be 9.33 kg/s, from the numerical calculations. Thus, as already mentioned before, the intake is operating in a subcritical mode for this free-stream Mach number.

Comparison of the ramp and lip wall pressure distribution (nondimensionalised with free-stream stagnation pressure) between numerical predictions and experimental data is given in Figs 5 and 6. The gradient-based adaption procedure has captured the shocks well, without any over/undershoot in the numerical solution, as can be seen in this figure.

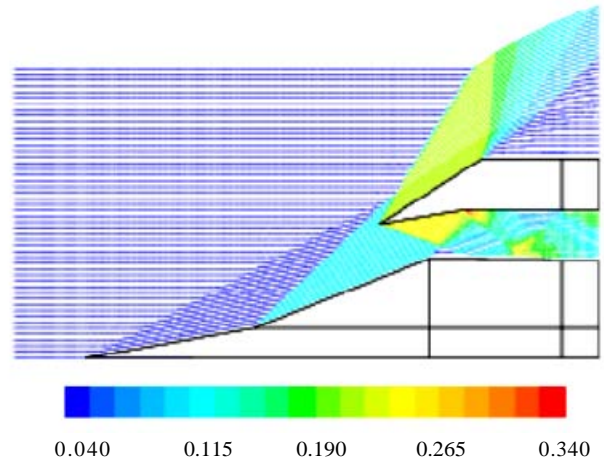


**Figure 4. Pathlines coloured by dimensionless static pressure.**

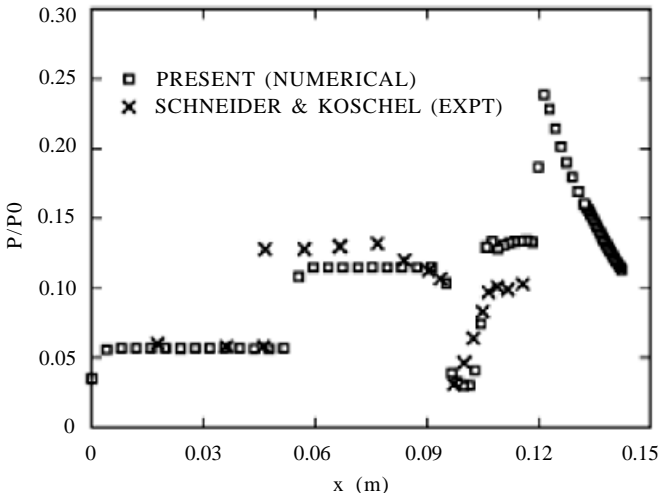


Figure 5. Variation of static pressure along the ramp

In this regard, it can also be noted that the spacing between the pressure taps on the lip wall in the experiment is such that the pressure rise due to the initial shock wave is highly under predicted. Nevertheless, the agreement between the numerical prediction and the experimental data is good, both in terms of the trends observed and the numerical values, with the maximum difference being of the order of 13 per cent. It should also be noted that the uncertainty in the experimental data is not known.

## 5. RESULTS AND DISCUSSION

### 5.1 Grid Independence Study

Calculations of the 3-D flow around the intake shown in Fig. 1 were initially carried out on a baseline grid (tetrahedral) with 338959 cells. This grid was refined next by adaption based on the gradient of static pressure, which resulted in a grid with 516710 cells. The area-averaged wall  $y^+$  for the converged solution on this grid was 272. This is only marginally better than the value of 325 on the previous grid, as the gradient adaption clusters the cells more along the flow direction. Refinement of this grid to reduce the wall  $y^+$  initially resulted in a grid with 825578 cells. The area-averaged wall  $y^+$  on this grid was 141, which is a significant improvement. Another level of refinement increased the grid size to 1270946 cells and reduced the wall  $y^+$  to 100, for the converged solution. For the standard wall function approach used here, this value of  $y^+$  is quite adequate<sup>9</sup> and so this grid has

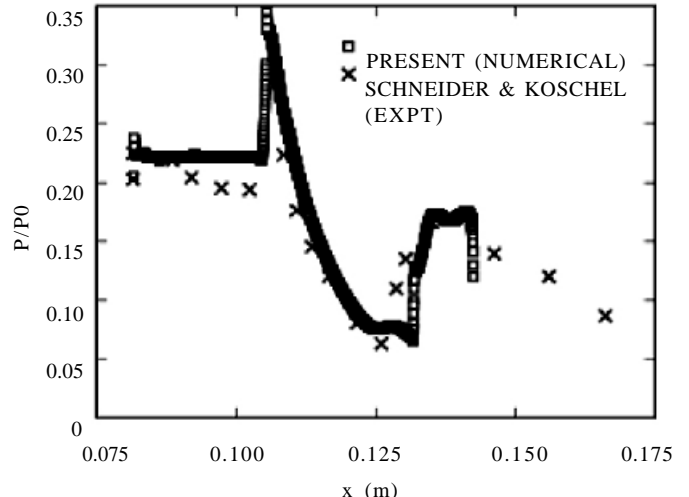


Figure 6. Variation of static pressure along the lip

been used for all the calculations. At each stage, the solution was taken to be converged when the mass imbalance in the entire computational domain as well as through the intake was  $< 0.1$  per cent of the respective mass flow rate.

### 5.2 Intake Flow Field and Performance Metrics

Contours of the gradient of pressure on the symmetry plane are shown in Figs 7 (a)-(e) for various angles of attack. Due to the finite radius of curvature of the nose portion of the forebody, a detached bowshock is generated ahead of the intake. This is followed by the oblique shocks originating from the compression ramps on the forebody. For  $8^\circ$  angle of attack, these shock waves intersect just at the leading edge of the engine bottom wall, and the inlet operates in the critical mode. It is to be noted that the intake is designed to be critical at  $6^\circ$  angle of attack. For lower angles of attack, the bowshock opens up and the point of intersection of the shock waves is ahead of the leading edge of the engine bottom wall and so there is spillage around the engine resulting in lower values for the mass flow rate, indicating subcritical operation. For angles of attack  $> 8^\circ$ , the bowshock can be seen to bend towards the forebody and the point of intersection of the shock moves slightly inside the engine intake. The spillage is also lower, and hence, the mass captured is higher. The intake operates in the supercritical mode for these angles of attack.

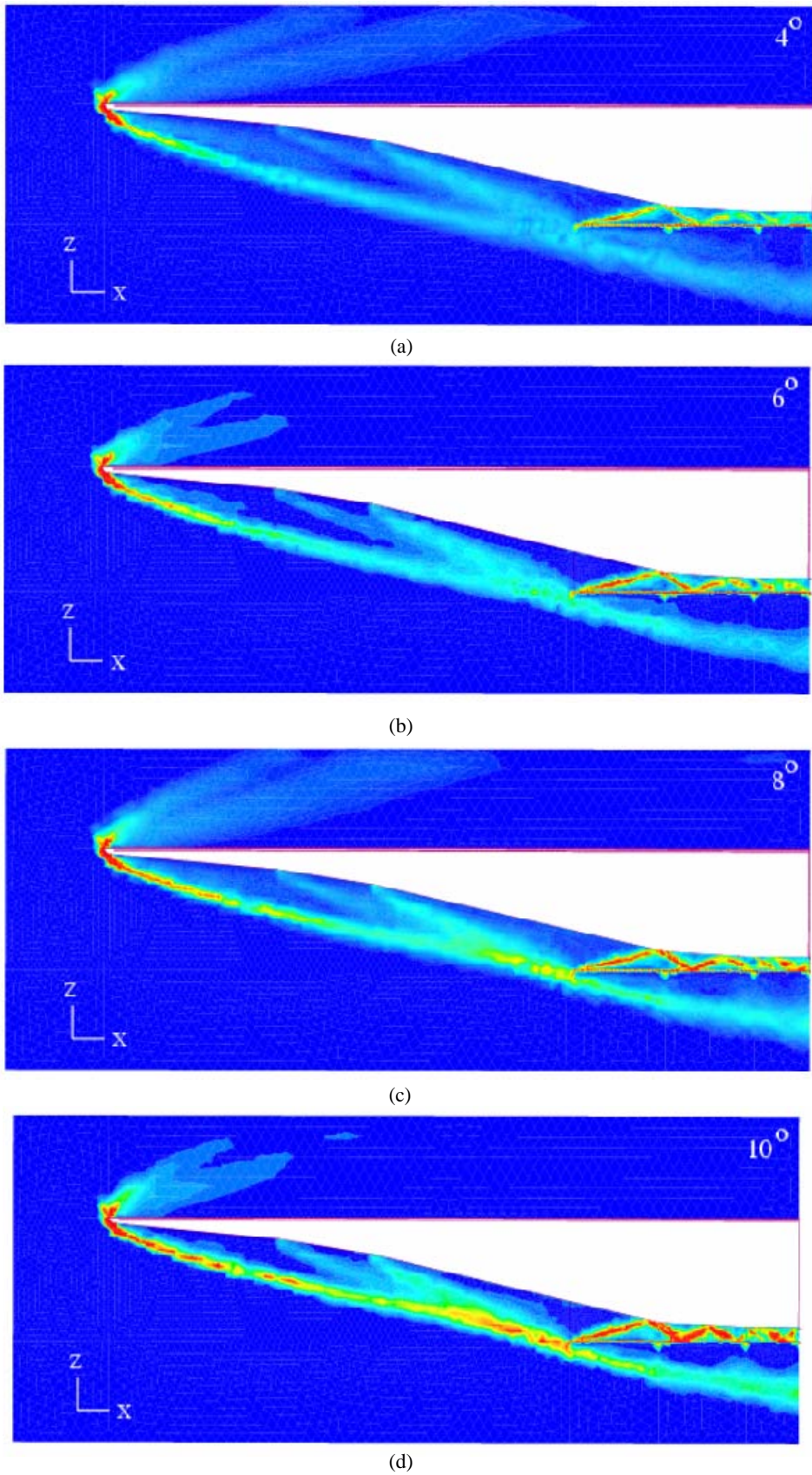
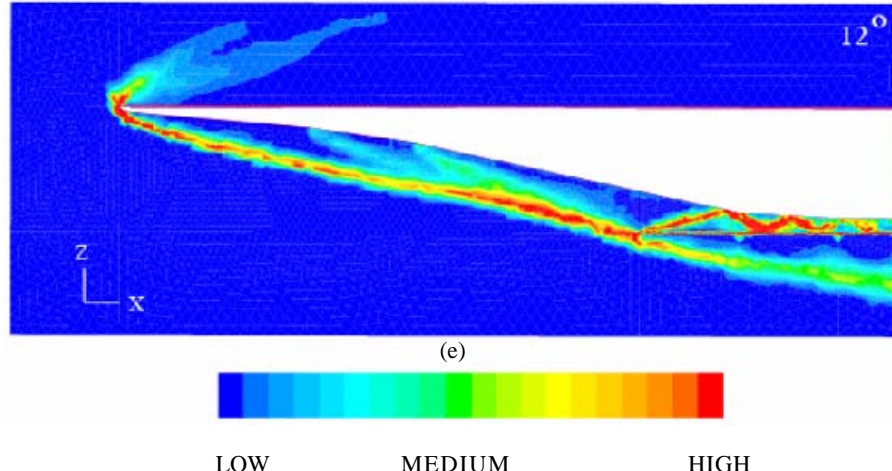
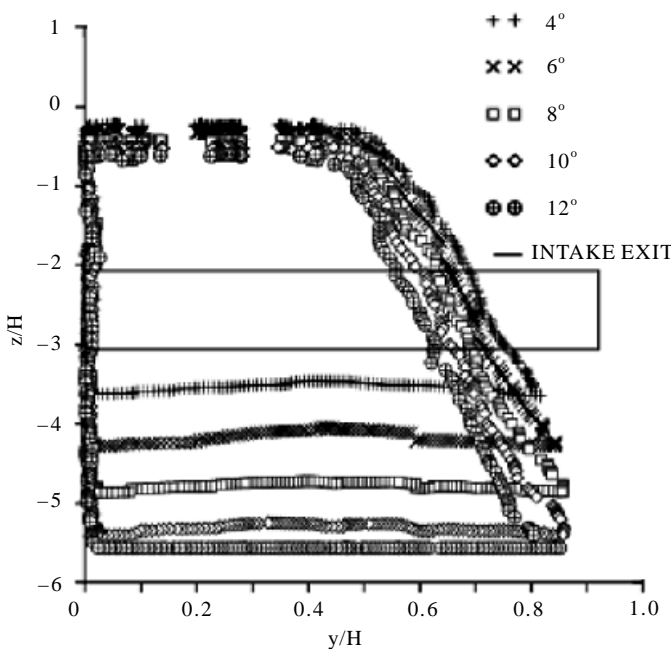


Figure 7 (a-d). Contours of gradient of static pressure on the symmetry plane for various angles of attack



**Figure 7 (e). Contours of gradient of static pressure on the symmetry plane for various angles of attack**

The trends for the mass flow rate captured by the engine at various angles of attack are illustrated in Fig. 8. Here, pathlines in the flow field that enter the engine have been used to show the free-stream capture area of the inlet. The cross-section at the inlet boundary of the streamtube that enters the engine inlet is shown in Fig. 8 for various angles of attack. The outline of the end of the inlet section is also shown in this figure for comparison. This figure clearly shows that the capture area, and hence the mass flow rate, increases with increasing



**Figure 8. Intake capture area for various angles of attack**

**Table 1. Operating conditions of the hypersonic vehicle**

Altitude (km)	32.5
Mach Number	6.5
Free stream static pressure (Pa)	830
Free stream static temperature (K)	230
Angle of attack (degree)	6

**Table 2.** Operating conditions for the 2-D intake

Mach number	2.99
Free stream static pressure (barr)	0.15
Free stream static temperature (K)	135
Angle of attack (degree)	0

angles of attack. However, the increase in the mass flow rate is smaller for the higher angles of attack (supercritical mode). Furthermore, the three-dimensionality of the flow field is clearly brought out in this figure, since the capture area and the outline of the inlet are both part of the same streamtube. There is considerable compression of the streamtube in the  $z$ -direction as a result of the leading edge bowshock as well as the shock waves from the ramps. It is interesting to see from this figure the expansion of the streamtube in the  $y$ -direction due to the three-dimensional relieving effect. Also, the expansion is more for the supercritical mode of operation. It should be noted that 2-D calculations can predict the compression but not the expansion of the streamtube.

It can be seen from Fig. 7 that the strength of the bowshock increases monotonically with the angle of attack. Also, the oblique shocks from the ramps as well the reflected shocks inside the engine show steeper gradients for the higher angles of attack. As a result, the Mach number at the inlet decreases (Table 3).

**Table 3. Mach number and flow distortion**

Angle of attack (degree)	Mach number at inlet		Flow distortion (%)
	Entry	Exit	
4	3.892	2.090	133
6	3.764	2.022	131
8	3.608	1.919	128
10	3.441	1.788	122
12	3.273	1.632	116

Also, the reduction in Mach number is more for the higher angles of attack. This implies that there is an optimum operating point at which the increased loss of stagnation pressure across the bowshock wave is offset by the reduced loss of stagnation pressure across the oblique shock waves due to the reduced Mach number. Stagnation pressure recovery for both the external and internal compression (Fig. 9) shows this to be true. While, the stagnation pressure recovery due to external compression is optimal for an angle of attack of  $6^\circ$ , it is poorer for the other angles of attack.

Stagnation pressure loss due to internal compression process is mainly due to viscous and boundary

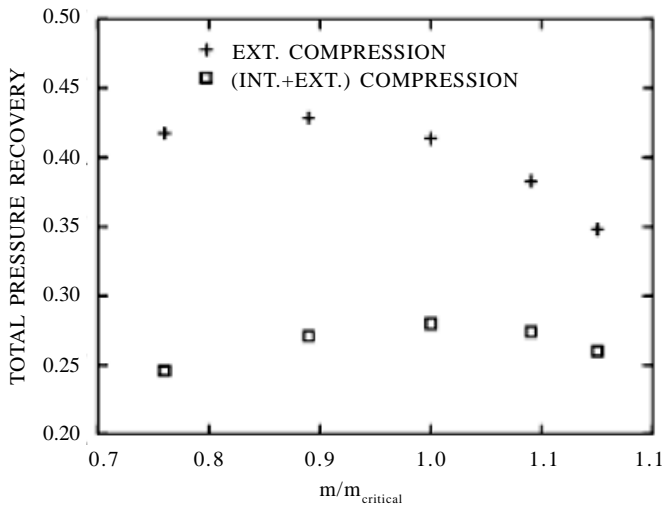


**Figure 9. Intake characteristic curve**

layer effects. Figure 9 shows that the stagnation pressure loss due to internal compression increases monotonically with angle of attack. However, the rate of increase is less than the corresponding rate due to external compression, and so the overall total pressure recovery shows an optimum at  $8^\circ$  angle of attack.

Calculated values of flow distortion at the inlet exit (Table 3) show the flow to be highly non-uniform.

Flow distortion at a given section is defined here in the usual manner as  $(P_{total, max} - P_{total, min}) = P_{total, mean}$ .

The flow distortion is  $> 120$  per cent for all the cases considered, whereas it is usually around 30 per cent or so for supersonic<sup>10</sup> intakes operating at intake Mach number around 2. Furthermore, the flow distortion decreases as the intake goes from subcritical to supercritical mode, which is quite opposite to the trend seen with supersonic intakes operating at lower Mach number<sup>10</sup>. It can be seen from the contours of  $(P_{total} - P_{total, mean}) = P_{total, mean}$  at the inlet exit shown in Fig. 10 that the spread in the total pressure decreases with increasing angle of attack. The extent of the core region, where the total pressure recovery is high, becomes smaller as the shock train inside the engine becomes stronger with increasing angles of attack.

### 5.3 Effect of Variable Properties

To determine the effect of variable properties calculations, calculations for an angle of attack at  $8^\circ$  were carried out free stream conditions for the constant property calculations were kept the same as those given in Table 1. Stagnation conditions, however, were different. Stagnation temperature and pressure are 1910 K and 1370 kPa for the variable property calculations, while these are 2170 K and 2142 kPa for the constant property calculations, with constant values for  $C_p$  and  $\gamma$ . Contours of the gradient of static pressure on the symmetry plane for this case (Fig. 11) show remarkable similarity to the corresponding variable property results. Mass flow rate through the engine is almost the same as before. Since, in reality,  $C_p$  increases with temperature,

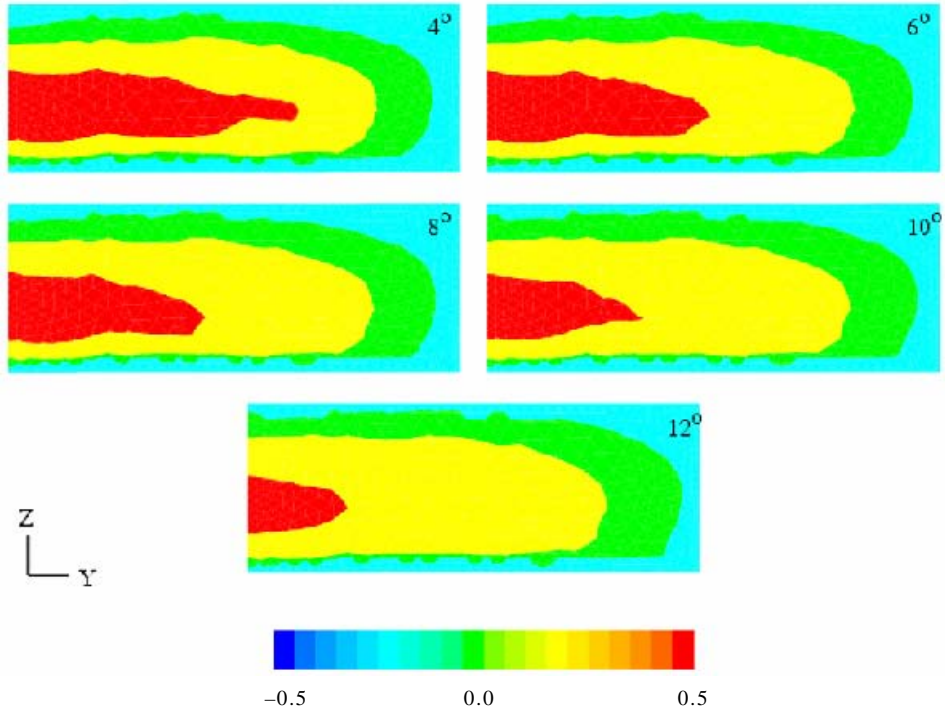


**Figure 10.** Contours of  $(P_{total} - P_{total, mean}) = P_{total, mean}$  at the inlet exit

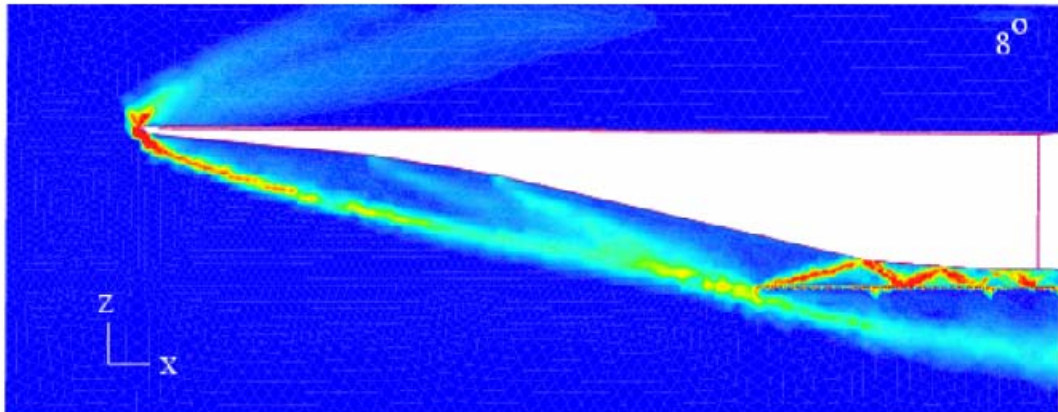


**Figure 11.** Contours of gradient of static pressure on the symmetry plane for 8° angle of attack with constant properties. Colour scale is the same as in Fig. 7.

constant property calculations always overpredict the static temperature. In the present case also, the maximum value for static temperature for the constant property calculations is 200 K higher than that of the variable property calculations. In addition, the total pressure recovery for the constant property calculations is 0.152 compared with 0.28 from before. Contours of  $P_{total} = P_{total, \infty}$  on the symmetry plane for both constant and variable property calculations shown in Fig. 12 reveal that the difference between

the two is more pronounced in regions of high temperature.

## 6. SUMMARY AND CONCLUSIONS

Numerical simulations of the compressible, 3-D non reacting flow in the engine inlet section of a concept hypersonic air-breathing vehicle are presented. These simulations have been carried out using FLUENT.

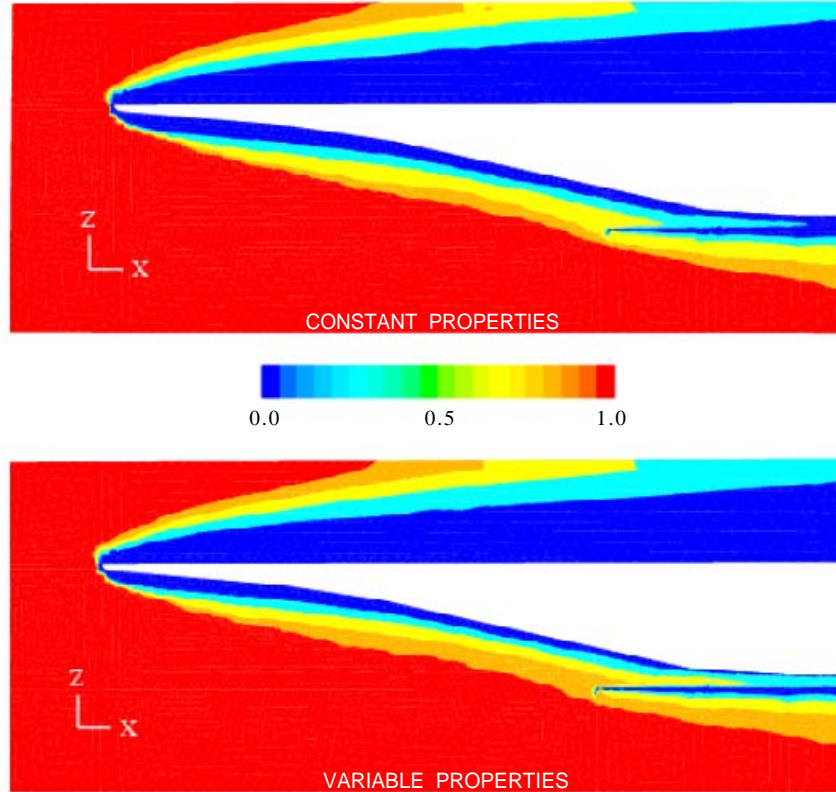


**Figure 12.** Contours of  $P_{total}/P_{total,\infty}$  on the symmetry plane for  $8^\circ$  angle of attack with constant and variable properties

The numerical methodology has been validated by simulating the flow through a 2-D mixed compression hypersonic intake model and comparing with experimental data. The calculations are shown to predict the locations and strengths of shock/expansion waves very well. For all the 3-D results reported, the mesh has been refined to achieve the area-averaged wall  $y+$  about 105. The characteristic curve obtained from the calculations indicate that the intake operates in the critical mode for an angle of attack at  $8^\circ$ . The calculations also show that the flow distortion at the intake exit is quite high for all the angles of attack considered. Numerically predicted free-stream capture area profiles, show the three-dimensionality of the flow field.

Comparison of the results from the variable and constant property calculations indicate that mass flow rate, and shock locations predicted by both to be almost the same. Whereas, static temperature and total pressure loss are overpredicted by the constant property calculations.

## ACKNOWLEDGMENTS

The authors would like to thank Dr S. Panneerselvam, Scientist G; Dr V. Ramanujachari, Scientist F; and Mr Ganesh Anavardham, Scientist D of Defence Research and Development Laboratory (DRDL), Hyderabad, for their help and valuable suggestions during the course of this study.

## REFERENCES

1. Gaitonde, D. & Shang, J.S. A numerical study of shock-on-shock viscous hypersonic flow past blunt bodies. *AIAA Paper No. 90- 1491*, 1990.
2. Schulte, D.; Henckels, A. & Wepler, U. Reduction of shock-induced boundary layer separation in hypersonic inlets using bleed. *Aero. Sci. Technol.*, 1998, **4**, pp. 231-39.
3. Schneider, A. & Koschel, W.W. Detailed analysis of a mixed compression hypersonic intake. International Society for Air Breathing Engines (ISABE), 1999, ISABE 99-7036.

4. Falempin, F. & Montazel, X. Investigation of two-mode ramjet/scramjet inlet. International Society for Air Breathing Engines (ISABE), 1999, ISABE 99-7040.
5. Goldfeld, M.A.; Nestoulia R.V. & Starov, A.V. Experimental study of scramjet module. International Society for Air Breathing Engines (ISABE), 1999, ISABE 99-7052.
6. Reddy, D.R. & Weir, L.J. Three-dimensional viscous analysis of a Mach 5 inlet and comparison with experimental data. *J. Prop. Power*, 1992, **8**(2), 432-40.
7. Bezgin, L.; Gouskov, O.; Kopchenov, V. & Laskin, I. CFD support of the development of hypersonic Flight laboratory and model scramjet. *AIAA*, 2002, AIAA Paper No. 2002-5125, .
8. Emami, S.; Trexler, C.A.; Auslender, A.H. & Weidner, J.P. Experimental investigation of inletcombustor isolators for a dual-mode scramjet at a Mach number of 4. May 1995, NASA Technical Paper No. NASA-TP-3502.
9. Rodriguez, C.G. & Cutler, A.D. Numerical analysis of the SCHOLAR supersonic combustor. NASA-CR-2003-212689, 2003.
10. Rajasingh Thangadurai, G.; Subhash Chandran, B.S.; Babu, V. & Sundararajan, T. Numerical investigations of the intake flow characteristics for a Ramjet engine with and without heat addition in the combustor. *Def. Sci. J.*, 2004, **54**(1), 3-16.

### Contributors



**Mr R. Sivakumar** obtained his MTech (Thermal Engg) from the Indian Institute of Technology (IIT) Madras, Chennai, in 2002. He worked as a Lecturer in Swamy Abethanandha Polytechnic College, Thellar, Tamilnadu, from 1995 to 2002. Currently, he is doing his PhD at IIT Madras. His research area include: Combustion instability in a bluff body combustor.



**Dr V. Babu** obtained his PhD (Mech) from the Ohio State University, USA, in 1991. Presently, he is working as Associate Professor at the IIT Madras. His areas of research include: Computational simulation of internal/ external flows, simulation of chemically reacting, plasma and nonequilibrium flows, high performance computing and development of software tools for engineering analysis. He is recipient of Henry Ford Technology Award (1998) presented by the Ford Motor Co. for the design, development and deployment of a virtual aerodynamic/aero-acoustic wind tunnel. He has four patents to his credit.